COUPLING OF PERIDYNAMIC THEORY
AND THE FINITE ELEMENT METHOD

Bahattin Kilic and Erdogan Madenci

COUPLING OF PERIDYNAMIC THEORY
AND THE FINITE ELEMENT METHOD

BAHATTIN KILIC AND ERDOGAN MADENCI

The finite element method is widely utilized for the numerical solution of structural problems. However, damage prediction using the finite element method can be very cumbersome because the derivatives of displacements are undefined at the discontinuities. In contrast, the peridynamic theory uses displacements rather than displacement derivatives in its formulation. Hence, peridynamic equations are valid everywhere, including discontinuities. Furthermore, the peridynamic theory does not require an external criterion for crack initiation and propagation since material failure is invoked through the material response. However, the finite element method is numerically more efficient than the peridynamic theory. Hence, this study presents a method to couple the peridynamic theory and finite element analysis to take advantage of both methods. The regions where failure is expected are modeled using peridynamics while remaining regions are modeled utilizing the finite element method. Finally, the present approach is demonstrated through a simple problem and predictions of the present approach are compared against both the peridynamic theory and finite element method. The damage simulation results for the present method are demonstrated by considering a plate with a circular cutout.

1. Introduction

Over the past several decades, the finite element method has become the most commonly accepted technique for the numerical solution of the equations of classical continuum mechanics. The success of the finite element method comes from its straightforward formulation, which primarily involves three basic steps. The first step is the approximate representation of the equations by either the variational or weighted residual method. The second step concerns construction of a system of governing algebraic equations by discretizing the region into finite elements. The last step involves the effective solution of the finite element equations. There are many commercial computer programs, such as ANSYS, ABAQUS, etc., and these programs enable the analysis of many engineering problems without much difficulty. However, the use of the finite element method can be quite challenging for damage prediction. This difficulty arises from the presence of spatial derivatives of displacements in the equations of classical continuum mechanics. These derivatives are undefined when the displacements are discontinuous, such as across cracks or interfaces. Hence, failure simulation based on stresses becomes invalid at these discontinuities because stresses asymptotically approach infinity. However, linear elastic fracture mechanics provides external failure criteria based on the stress intensity factor, energy release rate, etc.

Also, these criteria are often limited to the prediction of the smallest load for crack propagation and the direction of initial crack growth. In order to circumvent these shortcomings, the cohesive crack growth is introduced into the finite element method. As explained in [Moës and Belytschko 2002], there are

two main procedures for predicting crack growth: discrete interelement cracks and discrete intraelement cracks. In the interelement method, cohesive zone elements, as interelements, are placed in between each pair of neighboring elements in the mesh. However, these elements require a priori knowledge of the crack growth path, which might not be available unless an extremely fine mesh is employed.

The intraelement procedure incorporates a discontinuous mode at the element level and this method is used to model crack and shear band propagation. The use of an embedded discontinuous mode does not require remeshing but stability issues need to be considered in these methods [Moës and Belytschko 2002]. A comparative study of finite element methods with embedded discontinuous modes is given in [Jirásek 2000].

Belytschko and Black [1999] and Moës et al. [1999] introduced the extended finite element method X-FEM, which incorporates discontinuity in the displacement field along the crack path regardless of crack location and exploits the partition of the unity property of finite elements [Melenk and Babuška 1996]. In this method, the solution space is enriched by a priori knowledge about the behavior of the solution near any discontinuity and the additional number of degrees of freedom is minimized since the enrichment only includes the nodes that belong to the elements cut by cracks [Zi et al. 2007]. As explained in this last reference, there is a blending region that includes the neighboring elements of the tip element in which the crack tip is positioned. Partial enrichment exists for the elements in the blending region for which the partition of unity does not hold. Hence, the solution becomes inaccurate in the blending region.

Silling [2000], realizing the limitations, completely reformulated the basic equations of continuum mechanics. The resulting approach is known as the peridynamic theory. The main difference between the peridynamic theory and classical continuum mechanics is that the former utilizes displacement components without their spatial derivatives. This feature allows damage initiation and propagation at multiple sites with arbitrary paths inside the material without resorting to special crack growth criteria. In the peridynamic theory, internal forces are expressed through nonlocal interactions between pairs of material points within a continuous body, and damage is a part of this interaction. Interfaces between dissimilar materials have their own properties, and damage can propagate when and where it is energetically favorable for it to do so.

The peridynamic theory was utilized successfully for damage prediction of many problems. Silling [2003] considered the Kalthoff–Winkler experiment in which a plate having two parallel notches was impacted by a cylindrical impactor, and the peridynamic simulations successfully captured the angle of crack growth observed in the experiments. Impact damage was also predicted using peridynamics by Silling and Askari [2004; 2005]. This last paper considered a plate with a center crack to show the convergence of their numerical method. The peridynamic theory was applied to damage analysis of plain and reinforced concrete structures in [Gerstle and Sau 2004]. A new constitutive model was introduced for tearing and stretching of rubbery materials in [Silling and Askari 2005]. Using this model, they predicted oscillatory crack path when a blunt tool is forced through a membrane. The peridynamic theory was also applied successfully in [Askari et al. 2006] and [Colavito et al. 2007b] to predict damage in laminated composites subjected to low-velocity impact. Colavito et al. [2007a] used the peridynamic theory for damage prediction of woven composites subjected to static indentation. Xu et al. [2007] and Kilic [2008] considered notched laminated composites under biaxial loads.

Although the peridynamic theory provides deformation as well as damage initiation and growth without resorting to an external criterion, it is computationally more demanding than the finite element method

(FEM). Furthermore, the finite element method is very effective for modeling problems without damage. In order to take advantage of the computational robustness of FEM, Macek and Silling [2007] implemented the peridynamic model in a conventional finite element analysis code, ABAQUS by representing the peridynamic interactions with truss elements and using embedded element technique for the overlap region. However, the present study presents a direct approach to couple the peridynamic theory and finite element method to take advantage of their salient features. The regions involving failure are modeled using the peridynamic theory while the finite element method is utilized for the regions without failure. The coupling introduces an overlap region in which both the peridynamic and finite element equations are used simultaneously.

2. Peridynamic theory

The nonlocal peridynamic theory is concerned with the physics of a material body at a material point that interacts with all points within its range, as shown in Figure 1. As in the classical (local) continuum theory, the material points of a body are continuous, as opposed to discrete in the case of molecular dynamics. However, the main difference between the peridynamic and the classical continuum theories is that the former is formulated using integrodifferential equations, as opposed to partial differential equations that include spatial derivatives of the displacement components. Displacement derivatives do not appear in peridynamic equations, which allows the peridynamic formulation to be valid everywhere whether or not displacement discontinuities are present. As described in [Silling 2000], the peridynamic equation of motion at a reference configuration of position x and time t is given as

$$\rho \frac{\partial^2 u}{\partial t^2} = \int_{\mathscr{R}} dV_{x'} f\big(u(x,t), u(x',t), x', t\big) + b(x,t), \tag{1}$$

in which $\mathscr{R}$ is the domain of integration, u is the displacement vector field, b is a prescribed body-force density field, and ρ is mass density. The response function, f, is defined as the force vector per unit volume squared that the material point at x' exerts on the material point at x. The integral equation (1) represents a distinct mathematical system that is not derivable from the classical partial differential equations (PDEs).

2.1. *Response function.* Within the realm of the peridynamic theory, the material points interact with each other directly through a prescribed response function, which contains all the constitutive information associated with the material. The forces within the material are treated through interactions between pairs of material points in the continuum. The deformed position of a given material point is determined by the summation of forces between itself and all other material points with which it interacts. However, the response functions must obey the linear and angular admissibility conditions, which are examined in detail in [Silling 2000]. Any function satisfying the admissibility conditions is a valid response function. Therefore, the response functions are not restricted to be linear, which makes the peridynamic equation of motion given by (1) valid for both linear and nonlinear analyses. However, the response functions appearing in the literature and in this study assume pairwise interactions, which limits the Poisson's ratio to 0.25. Also, the limiting values of the Poisson's ration under plane stress and plane strain assumptions are explained in [Gerstle et al. 2005]. The response function relates the dependence of the interaction force on reference positions and displacements of any material point pairs. This interaction force can also
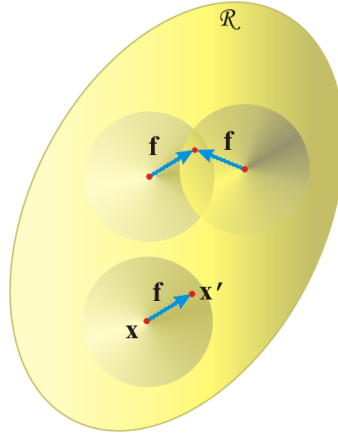
Figure 1. Pairwise interaction of a material point with its neighboring points.

be viewed as a bond force between the material points. The present study utilizes the response function described in [Kilic 2008], which can be written as

$$f(\eta, \xi) = \frac{\xi + \eta}{|\xi + \eta|} \mu(\xi, t) \frac{9k}{\pi l^4} e^{-(|\xi|/l)^2} s, \tag{2}$$

in which k is the bulk modulus and l is the internal length, which is the measure of nonlocal behavior. The locality of interactions depends on the internal length l and interactions become more local with decreasing internal length, as shown in Figure 2. The relative position, ξ, can be expressed as $\xi = x' - x$ in the reference configuration, as illustrated in Figure 3. The relative displacement, η, can be written as
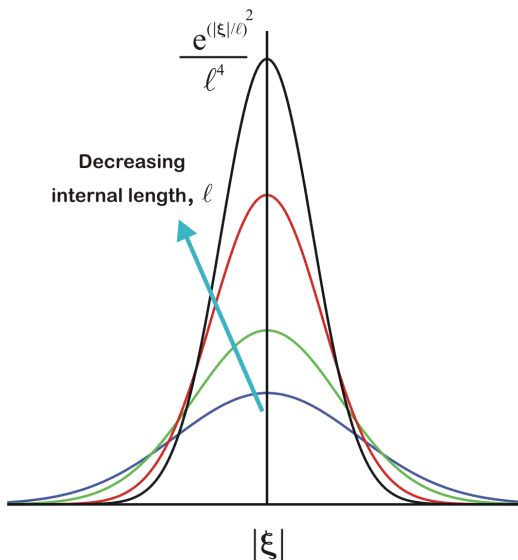
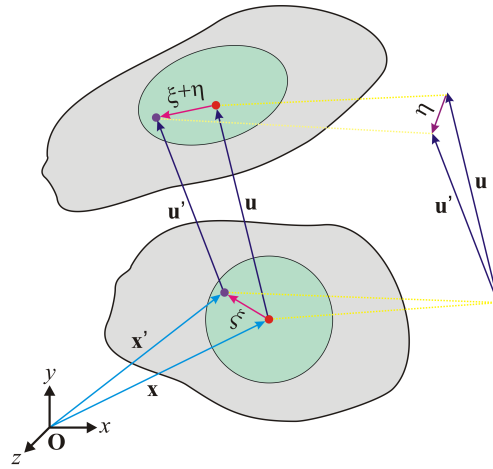**Figure 2.** Effect of internal length on the locality of interactions.

Figure 3. Definition of geometric parameters.

$\boldsymbol{\eta} = \boldsymbol{u}' - \boldsymbol{u}$ between points $\boldsymbol{x}'$ and $\boldsymbol{x}$, as shown in Figure 3. The stretch, s, is given as

$$s = \frac{|\boldsymbol{\xi} + \boldsymbol{\eta}| - |\boldsymbol{\xi}|}{|\boldsymbol{\xi}|} \tag{3}$$

and it is the ratio of the change in distance to initial distance between points $\boldsymbol{x}'$ and $\boldsymbol{x}$. Failure is included in the material response through a history-dependent scalar-valued function μ (see [Silling and Bobaru 2005]), defined as

$$\mu(\boldsymbol{\xi}, t) = \begin{cases} 1 & \text{if } s(t', \boldsymbol{\xi}) < s_0 \text{ for all } 0 < t' < t, \\ 0 & \text{otherwise,} \end{cases} \tag{4}$$

in which s_0 is the critical stretch for failure to occur, as shown in Figure 4. In the solution phase, the displacements and stretches between pairs of material points are computed. When the stretch between two points exceeds the critical stretch, s_0, failure occurs and these two points cease to interact. As derived in [Silling and Askari 2005], the critical stretch value can be related to the well-known fracture parameters such as the energy release rate. Thus, damage in a material is simulated in a much more realistic manner
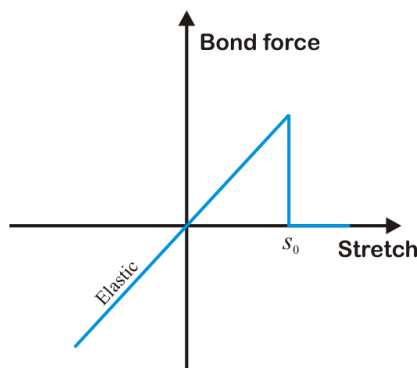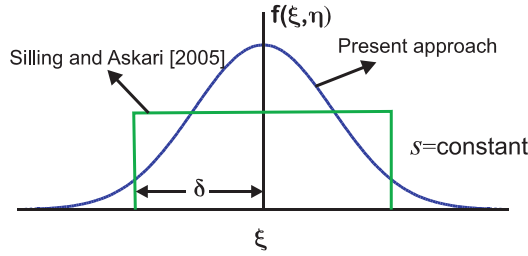

Figure 4. Model for bond failure.

Figure 5. Comparison of response functions under constant stretch.

compared to the classical continuum-based methods. The inexplicit nature of local damage at a point, arising from the introduction of failure in the constitutive model, is removed by defining the local damage as

$$\varphi(x, t) = 1 - \frac{\int_{\mathcal{R}} dV_{x'} \mu(t, \boldsymbol{\xi}) e^{-(|\boldsymbol{\xi}|/l)^2}}{\int_{\mathcal{R}} dV_{x'} e^{-(|\boldsymbol{\xi}|/l)^2}}. \tag{5}$$

Thus, the local damage is the weighted ratio of the amount of the broken interactions to the total amount of interactions.

The present response function is more complicated than that given in [Silling and Askari 2005] due to the exponential term in (2). The behavior of this response function under constant stretch is illustrated in Figure 5. As shown in this figure, Silling and Askari's response function suggests that interaction force remains the same within the horizon regardless of the distance between the interacting points. However, the forces acting among bodies decrease with increasing distances. Hence, present method utilizes the response function in (2) in which interaction force decreases with increasing distance between the two material interaction points.

Because the peridynamic theory is nonlocal, material points interact across the interfaces. Hence, the response function needs to be specified for the interface, in addition to the response functions for individual materials. Therefore, the peridynamic theory is capable of modeling different adhesion strengths of the materials. If the domain consists of two dissimilar materials (Figure 6), three different interactions need to be specified. Two of these interactions occur between material points having the same material, labeled 1 and 2 in the figure, and the material properties used by the response function are trivially chosen to be those of the material point. In the case of interactions across the interface, labeled 3, the numerical experiments revealed that displacement predictions are insensitive to properties of the interface material if the numbers of interactions across the interfaces are much smaller than those for material points having the same material. Also, when the numbers of interactions across the interfaces are comparable to those
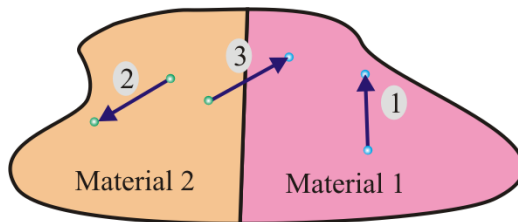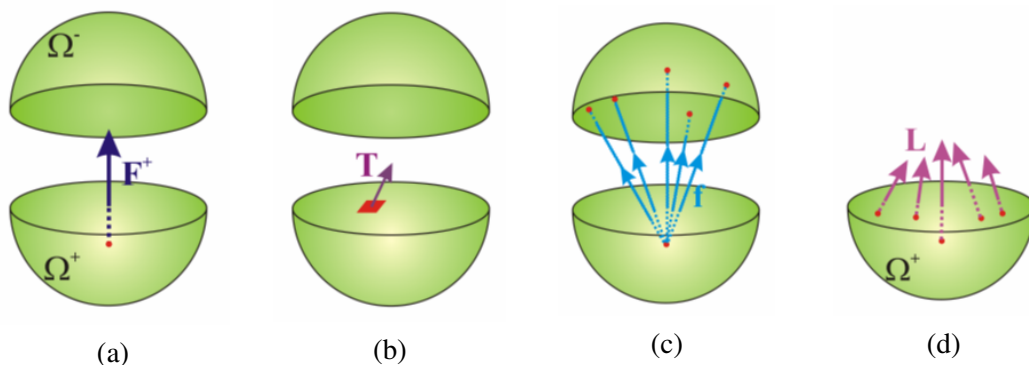

Figure 6. Interactions among material points.

Figure 7. Boundary conditions: (a) domain of interest; (b) tractions in classical continuum mechanics; (c) interaction of a point in the domain Ω^+ with the domain Ω^-; (d) force densities acting on the domain Ω^+ due to the domain Ω^-.

between the material points having the same material the use of the smaller of the bulk moduli of the two materials gives better results. Hence, the response function for interactions across the interface utilizes the material properties of the region having the smaller bulk modulus.

2.2. *Boundary conditions.* Since peridynamics is a nonlocal theory and its equations of motion utilize integrodifferential equations as opposed to partial differential equations in the case of the classical continuum theory, the application of boundary conditions is also very different from that of the classical continuum theory. The difference can be illustrated by considering a body that is subjected to mechanical loads. If this body is fictitiously divided into two domains, Ω^- and Ω^+ as shown in Figure 7a, there must be a net force, $\boldsymbol{F}^+$, that is exerted to domain Ω^+ by domain Ω^- so that force equilibrium is satisfied.

According to the classical continuum mechanics, the force $\boldsymbol{F}^+$ can be determined by integrating surface tractions over the cross section area, $\partial\Omega$, of the domains Ω^- and Ω^+:

$$\boldsymbol{F}^+ = \int_{\partial\Omega} dA \, \boldsymbol{T}, \tag{6}$$

in which $\boldsymbol{T}$ denotes the surface tractions (Figure 7b). In the case of the peridynamic theory, the material points located in Ω^+ interact with the other material points in Ω^- (Figure 7c). Hence, the force densities, $\boldsymbol{L}$, acting on points in Ω^+ must be determined by integrating the response function over Ω^-:

$$\boldsymbol{L}(\boldsymbol{x}) = \int_{\Omega^-} dV \, \boldsymbol{f}(\boldsymbol{x}, \boldsymbol{x}'). \tag{7}$$

Finally, the force $\boldsymbol{F}^+$ can be computed by volume integration of these force densities (Figure 7d) over Ω^+:

$$\boldsymbol{F}^+ = \int_{\Omega^-} dV \, \boldsymbol{L}(\boldsymbol{x}). \tag{8}$$

Hence, the tractions or point forces cannot be applied as boundary conditions since their volume integrations result in a zero value. Therefore, the boundary conditions are applied over the volumes as body forces, displacements, and velocities.

3. Numerical implementation

In order to solve (1), a collocation method is adopted and the numerical treatment involves the discretization of the domain of interest into subdomains (Figure 8). Collocation (integration) points are subsequently placed into subdomains in order to reduce the peridynamic equation of motion into a finite sum as

$$\rho \ddot{\boldsymbol{u}}(\boldsymbol{x}_i, t) = \boldsymbol{b}(\boldsymbol{x}_i, t) + \sum_{e=1}^{N} \sum_{j=1}^{N_e} w_j \boldsymbol{f}\left(\boldsymbol{u}(\boldsymbol{x}_i, t), \boldsymbol{u}(\boldsymbol{x}'_k, t), \boldsymbol{x}_i, \boldsymbol{x}'_k, t\right), \tag{9}$$

where $\boldsymbol{x}_i$ is the position vector located at the i-th collocation point, N is the number of subdomains, and N_e is the number of collocation points in the e-th subdomain. The position vector $\boldsymbol{x}'_k$ represents the j-th integration point of the e-th subdomain. The parameter w_j is the integration weight of the point $\boldsymbol{x}'_k$. Present discretization becomes identical to that given in [Silling and Askari 2005] when the number of collocation points is set to 1.

In this study, volume integration is performed using hexahedron-shaped subdomains utilizing eight integration points. This type of discretization leads to a large number of collocation points in some problems. Therefore, parallel processing using OpenMP is also employed to reduce computation time while utilizing uniform grids as arrays of linked lists as described in [Kilic 2008]. A binary space
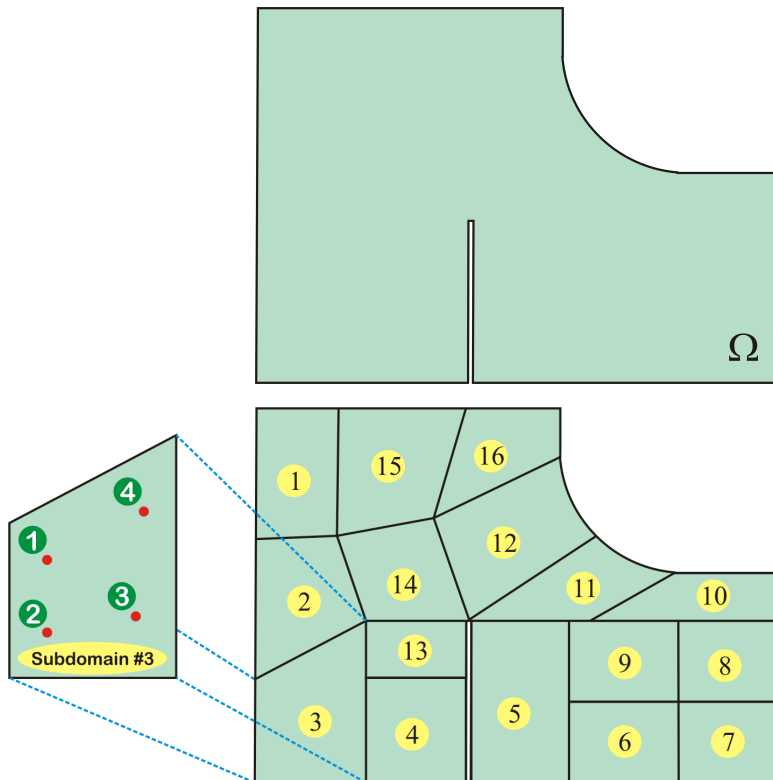

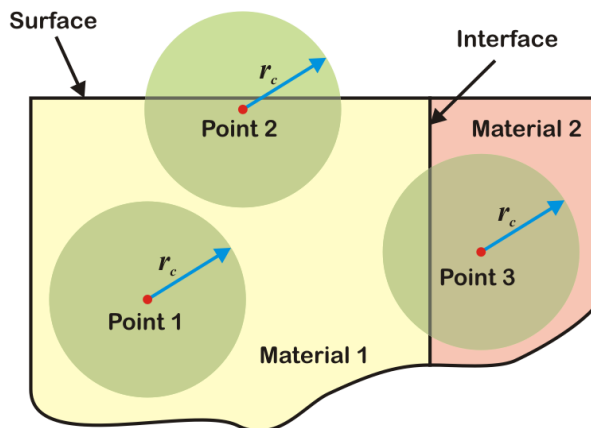**Figure 8.** Discretization of the domain of interest.

Figure 9. Surface effects in the domain of interest.

decomposition introduced in [Berger and Bokhari 1987; Kilic 2008] is used to obtain good load balancing on each processor. The decomposition involves division of the space into two subunits, with an approximately equal number of collocation points. Each subunit is then continuously divided into two subunits until the number of subunits and processors become equal. Division is performed only on the x-, y-, or z-plane, with the constraint of minimum division surface to reduce the communication cost among the processors.

Also, the response function given by (2) is derived with the assumption that the point located at x is in an infinite domain consisting of a single material. However, this assumption becomes invalid when the material point is close to free surfaces or material interfaces (Figure 9). Therefore, there is a reduction in material stiffness near the free surfaces. On the other hand, stiffness near the interface can exhibit an increase or reduction, depending upon how dissimilar material regions interact across their interface. Since free surfaces and material interfaces vary from one problem to another, it is impractical to resolve this issue analytically. Therefore, the stiffness reduction or increase due to surfaces is corrected numerically as explained in Appendix A.

The problems considered herein necessitate the determination of steady-state and quasistatic solutions. However, the system of ordinary nonlinear differential equations given in (9) includes dynamic terms that need to be eliminated. Thus, the adaptive dynamic relaxation method given in [Kilic 2008] is utilized to obtain a steady-state solution. The dynamic relaxation method is based on the fact that the static solution is the steady-state part of the transient response of the solution. An artificial damping is introduced to guide the solution into the steady-state regime as fast as possible. Although this method is successfully utilized by Silling and his coworkers in the Emu code, it is not always possible to determine the most effective damping coefficient. Alternate to the numerical (artificial) damping, Underwood [1983] introduced an adaptive dynamic relaxation method in which the damping coefficient is changed adaptively in each time step. This method was recently extended in [Kilic 2008] for the solution of peridynamic equations in the present numerical method in which (9) is modified at time step n as

$$\ddot{U}^n(X, t_n) + c\dot{U}^n(X, t_n) = \Lambda^{-1} F^n(U^n, U'^n, X, X'), \tag{10}$$

in which c is the damping coefficient and $\mathbf{\Lambda}$ is the fictitious diagonal density matrix that is expressed in [Kilic 2008] as

$$\lambda_{ii} \geq \frac{1}{4} \Delta t^2 \max\left(\sum_{e=1}^{N} \sum_{j=1}^{N_e} \mathrm{abs}(\boldsymbol{\xi}) w_j \frac{18k}{\pi l^4} e^{-(|\boldsymbol{\xi}|/l)^2} \frac{1}{|\boldsymbol{\xi}|^2}\right), \tag{11}$$

where max is the function that returns the value of the maximum component of the three-dimensional vector in its argument. Hence, the densities associated with a particular material point are the same in every direction of the coordinate frame, making them frame invariant. The function $\mathrm{abs}(\cdot)$ returns a three-dimensional vector whose components are the absolute values of the three components of the vector in its argument. The vectors $\boldsymbol{X}$ and $\boldsymbol{U}$ represent positions and displacements at the collocation points, respectively, and they can be expressed as

$$\boldsymbol{X}^T = \{\boldsymbol{x}, \boldsymbol{x}_2, \ldots, \boldsymbol{x}_M\}, \tag{12}$$

$$\boldsymbol{U}^T = \{\boldsymbol{u}(\boldsymbol{x}_1, t), \boldsymbol{u}(\boldsymbol{x}_2, t), \ldots, \boldsymbol{u}(\boldsymbol{x}_M, t)\}, \tag{13}$$

where M is the total number of collocation points. Finally, the vector $\boldsymbol{F}$ is the summation of internal and external forces, and its i-th component can be written as

$$\boldsymbol{F}_i = \boldsymbol{b}(\boldsymbol{x}_i, t) + \sum_{e=1}^{N} \sum_{j=1}^{N_e} w_j \boldsymbol{f}(\boldsymbol{u}(\boldsymbol{x}_i, t), \boldsymbol{u}(\boldsymbol{x}'_k, t), \boldsymbol{x}_i, \boldsymbol{x}'_k, t)). \tag{14}$$

3.1. Finite element equations. The theory for the development of the finite element method is well established [Belytschko 1983; Bathe 1982; Zienkiewicz 1977]; however, this section briefly describes the assembly of finite element equations and the solution of the assembled equations using the adaptive dynamic relaxation technique. The finite element formulation utilized in this study can be found in most finite element textbooks such as [Zienkiewicz 1977]. Hence, details will not be given here but the interested reader can refer to [Kilic 2008]. The present study utilizes direct assembly of finite element equations without constructing the global stiffness matrix. Hence, the element stiffness vector can be expressed as

$$\boldsymbol{f}^{(e)} = \boldsymbol{k}^{(e)} \boldsymbol{u}^{(e)}, \tag{15}$$

in which $\boldsymbol{k}^{(e)}$ is the element stiffness matrix described in [Zienkiewicz 1977] and $\boldsymbol{u}^{(e)}$ is the vector representing the nodal displacements of the e-th element. The element stiffness vector, $\boldsymbol{f}^{(e)}$, includes internal forces resulting from the deformation of the element. They can be assembled into a global array of internal forces by using the convention of [Belytschko 1983] as

$$\boldsymbol{f}^{\mathrm{int}} = \underset{e}{A} \boldsymbol{f}^{(e)}, \tag{16}$$

where A is the assembly operator. These operations are strictly performed as additions. Finally, the equations of motion for adaptive dynamic relaxation can be written as

$$\ddot{\boldsymbol{u}}^n + c_n \dot{\boldsymbol{u}}^n = \boldsymbol{M}^{-1} \boldsymbol{F}^n, \tag{17}$$

in which $\boldsymbol{M}$ is the mass matrix, c is the damping coefficient, and n indicates the n-th time increment. The force vector $\boldsymbol{F}$ can be expressed as

$$\boldsymbol{F}^n = \boldsymbol{f}^{\mathrm{ext}}(t^n) - \boldsymbol{f}^{\mathrm{int}}(\boldsymbol{u}^n) \tag{18}$$

where t is time and $\boldsymbol{f}^{\text{ext}}$ is the vector of external forces. As suggested in [Underwood 1983], components of the diagonal mass matrix can be effectively computed using

$$m_{ii} \geq \frac{1}{4}\Delta t^2 \sum_j |K_{ij}|, \tag{19}$$

where K_{ij} is the global stiffness matrix. However, the global stiffness matrix necessitates the use of a large amount of computer memory, which is herein avoided by constructing the mass matrix approximately as

$$\boldsymbol{M} = \boldsymbol{I}\tilde{\boldsymbol{m}}, \tag{20}$$

in which $\boldsymbol{I}$ is the identity matrix. The mass vector, $\tilde{\boldsymbol{m}}$, is constructed as

$$\tilde{\boldsymbol{m}} = \underset{e}{\boldsymbol{A}} \, \hat{m}^{(e)}, \tag{21}$$

where the components of vector $\hat{\boldsymbol{m}}^{(e)}$ can be written as

$$\hat{m}_i^{(e)} = \sum_{j=1}^{8} |k_{ij}^{(e)}|, \tag{22}$$

in which $k_{ij}^{(e)}$ indicates the components of the element stiffness matrix given in [Zienkiewicz 1977]. This approach for the construction of a mass matrix is not as effective as that given in (19). However, it is not intended in this study to present a numerically efficient adaptive dynamic relaxation method for the finite element method; the choice of this method is solely based on simplicity of the numerical implementation. The components of the mass matrix given in (20) always satisfy the inequality given in (19) because the construction of the global matrix involves addition of positive and negative values and the present approach uses summation of their absolute values.

3.2. *Coupling of peridynamic theory and finite element method.* In order to take full advantage of the peridynamic theory and finite element method, the domain of interest is partitioned into two regions. These regions are modeled using the finite element method and the peridynamic theory, as shown in Figure 10a. In order to reduce the peridynamic equation of motion to its discrete form, the peridynamic region is discretized into subdomains (Figure 10b), and Gaussian integration points are placed into each subdomain (Figure 10b). As explained in [Kilic 2008], subdomains with different shapes can be utilized during the discretizations. However, this study only considers subdomains with a hexahedral shape and volume integration is performed by employing eight integration points.

According to the response function given in (2), a material point interacts with all other points within the problem domain. However, it is computationally expensive to include the interaction of a large number of collocation points. As shown in Figure 2, the magnitude of the response function fortunately decreases rapidly when the distance between the points increases. Thus, a cutoff radius, r_c, is introduced to reduce the computation time by limiting the interaction range (described in detail in [Kilic 2008]). However, the internal length, l, cannot be chosen arbitrarily small since the accuracy of volume integrals in (1) is dependent on the variation of the response function within the subdomains. Kilic [2008] numerically investigated the effect of the internal length and cutoff radius on the numerical predictions in detail.
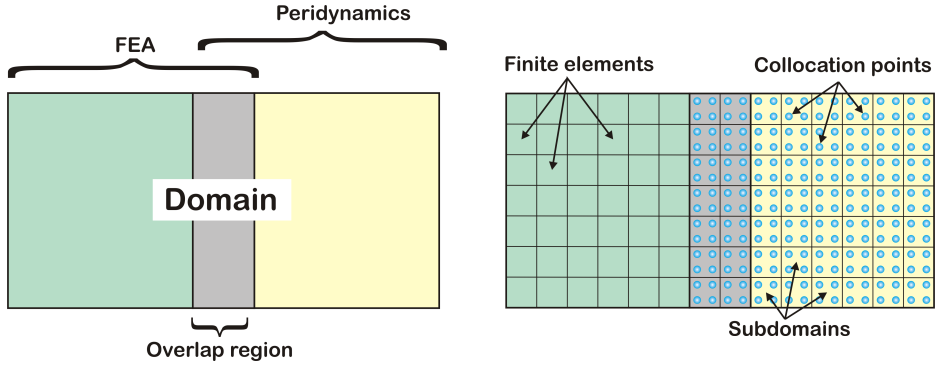
Figure 10. Schematic for coupling of the finite element method and peridynamics. Left: finite element (FEA) and peridynamic regions. Right: discretization.

Based on his findings, the internal length, l, is chosen to be approximately the maximum edge length of the hexahedral subdomains and the cutoff radius, r_c, is then set to 2.5 times the internal length, l.

The finite element region is also discretized to construct (17) by using hexahedral elements (Figure 10, right). In the region of overlap shown in Figure 10, left, both the peridynamic and the finite element equations are utilized. to achieve the appropriate coupling, the discrete peridynamic equation of motion is rewritten as

$$\begin{Bmatrix} \ddot{\underline{U}}_p^n \\ \ddot{\underline{\underline{U}}}_p^n \end{Bmatrix} + c_n \begin{Bmatrix} \dot{\underline{U}}_p^n \\ \dot{\underline{\underline{U}}}_p^n \end{Bmatrix} = \begin{bmatrix} \boldsymbol{\Lambda}^{-1} & 0 \\ 0 & \underline{\boldsymbol{\Lambda}}^{-1} \end{bmatrix} \begin{Bmatrix} \underline{F}_p^n \\ \underline{\underline{F}}_p^n \end{Bmatrix}, \tag{23}$$

where U is a vector that contains displacements at the collocation points, subscript p denotes the variables associated with the peridynamic region, and single and double underscores denote the variables located outside and inside the overlap region, respectively. The finite element equations are also rewritten as

$$\begin{Bmatrix} \ddot{\underline{U}}_f^n \\ \ddot{\underline{\underline{U}}}_f^n \end{Bmatrix} + c_n \begin{Bmatrix} \dot{\underline{U}}_f^n \\ \dot{\underline{\underline{U}}}_f^n \end{Bmatrix} = \begin{bmatrix} \boldsymbol{M}^{-1} & 0 \\ 0 & \underline{\boldsymbol{M}}^{-1} \end{bmatrix} \begin{Bmatrix} \underline{F}_f^n \\ \underline{\underline{F}}_f^n \end{Bmatrix}, \tag{24}$$

in which subscript f denotes the variables associated with the finite element region. The solution vector $\dot{\underline{U}}_p$, representing displacements at the collocation points, is expressed in terms of the solution vector $\dot{\underline{\underline{U}}}_f^n$, denoting nodal displacements of finite element interpolation functions, as

$$\boldsymbol{u}_p = \sum_{i=1}^{8} N_i \boldsymbol{u}_i^{(e)} \tag{25}$$

where N_i are the shape functions given in [Zienkiewicz 1977]. The vector $\boldsymbol{u}_i^{(e)}$ is the i-th nodal displacements of the e-th element and it is extracted from the global solution vector, $\underline{U}_f$. The vector $\boldsymbol{u}_p$ represents displacements of a collocation point located inside the e-th element. Since vector $\underline{\underline{U}}_p$ can be computed using (25), the force density vector $\underline{\underline{F}}_p^n$ can then be computed by utilizing (14). Furthermore, the body force densities at the collocation points are lumped into the nodes as

$$\boldsymbol{f}_I^{(e)} = \int_{V_e} dV_e N_I \rho \, \boldsymbol{g} \tag{26}$$

in which ρ is the mass density of the e-th element, $\boldsymbol{g}$ is the body force density, and I indicates the I-th node of the e-th element. Hence, $f_i^{(e)}$ indicates the external force acting on the I-th node. The body force density is only known at the collocation points. Fortunately, the collocation points are placed by using a Gaussian integration technique. This allows the numerical evaluation of (26) by using collocation points as integration points for the e-th element. Furthermore, $\underline{\underline{F}}_f^n$ is constructed by assembling the nodal forces given by (26). Finally, the coupled system of equations can be expressed as

$$\ddot{\underline{U}}^n + c_n \dot{\underline{U}}^n = \underline{M}^{-1} \underline{F}^n, \tag{27}$$

in which

$$\dot{\underline{U}} = \{\dot{\underline{U}}_p^n \quad \dot{\underline{U}}_f^n \quad \dot{\underline{\underline{U}}}_f^n\}^T \quad \text{and} \quad \ddot{\underline{U}} = \{\ddot{\underline{U}}_p^n \quad \ddot{\underline{U}}_f^n \quad \ddot{\underline{\underline{U}}}_f^n\}^T \tag{28}$$

are the first and second time derivatives of the displacements, the matrix $\underline{M}$ is given by

$$\underline{M} = \begin{bmatrix} \boldsymbol{\Lambda} & 0 & 0 \\ 0 & \boldsymbol{M} & 0 \\ 0 & 0 & \underline{M} \end{bmatrix}, \tag{29}$$

and the vector $\underline{F}$ by

$$\underline{F}^n = \{\underline{F}_p^n \quad \underline{F}_f^n \quad \underline{\underline{F}}_f^n\}^T. \tag{30}$$

As suggested in [Underwood 1983], the damping coefficient c_n can be written as

$$c_n = 2\sqrt{\left((\underline{U}^n)^T \, {}^1\boldsymbol{K}^n \underline{U}^n\right) \Big/ \left((\underline{U}^n)^T \, \underline{U}^n\right)} \tag{31}$$

in which ${}^1\boldsymbol{K}^n$ is the diagonal "local" stiffness matrix expressed as

$$^1K_{ii}^n = -\left(\underline{F}_i^n / \underline{m}_{ii} - \underline{F}_i^{n-1} / \underline{m}_{ii}\right) \Big/ \dot{U}_i^{n-1/2} \tag{32}$$

(see [Underwood 1983]). The time integration is performed using central-difference explicit integration, with a time step size of unity; explicitly,

$$\dot{\underline{U}}^{n+1/2} = \left((2 - c_n)\dot{\underline{U}}^{n-1/2} + 2\underline{M}^{-1}\underline{F}^n\right) \big/ (2 + c_n), \tag{33}$$

$$\underline{U}^{n+1} = \underline{U}^n + \dot{\underline{U}}^{n+1/2}. \tag{34}$$

However, the integration algorithm given by (33) and (34) cannot be used to start the integration due to an unknown velocity field at $t^{-1/2}$. Integration can be started by assuming that $\underline{U}^0 \neq 0$ and $\dot{\underline{U}}^0 = 0$:

$$\dot{\underline{U}}^{1/2} = \tfrac{1}{2}\underline{M}^{-1}\underline{F}^{1/2}. \tag{35}$$

4. Numerical results

The present approach is demonstrated by considering a bar subjected to tension and a plate with a circular cutout. The bar under tension is considered to compare the displacements of the present coupled analysis, the peridynamic theory, and finite element methods while not allowing for failure to occur. The damage prediction capability of the coupled analysis is then illustrated by considering a plate with a circular cutout. Although the numerical values of the material properties are representative of engineering materials, they are not specific to a particular material. Also, the effects of the peridynamic parameters
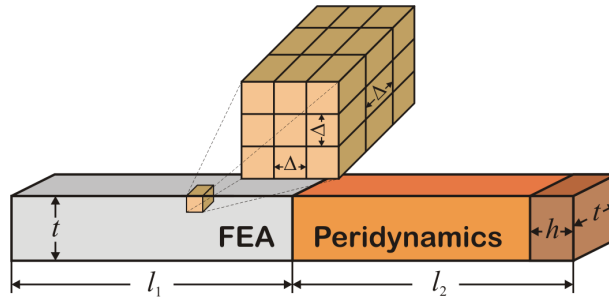
Figure 11. Dimensions and discretization of the bar.

and discretization on the convergence of the results are established by considering a rectangular plate subjected to uniaxial tension. The details of this convergence study are given in Appendix B.

4.1. *Bar subjected to tension.* Figure 11 describes the geometry of a bar having square cross section. The material is isotropic with Young's modulus and Poisson's ratio of $E = 10^7$ psi and $\nu = 0.25$, respectively. The bar is divided into two regions, which are modeled by using the finite element method and peridynamic theory. Furthermore, the lengths of these regions are specified to be $l_1 = 5$ in and $l_2 = 5$ in for the finite element and peridynamic regions, respectively. The bar has a square cross section with an edge length of $t = 0.4$ in. Moreover, the bar is free of any displacement constraints and subjected to uniaxial tension of 1600 lb. Because of the nonlocal nature of peridynamics, the point and surface loads cannot be applied directly. Hence, the body force density term in (1) is utilized to act as a uniaxial tension. Rectangular volume at the end of the bar is then subjected to the uniform body force density of 2×10^5 lb/in^3, and its length is chosen to be $h = 0.05$ in. In the case of a finite element region, the tensile load is applied as uniform point forces on the nodes located at the surface of the bar.

The three-dimensional model is constructed to obtain a steady-state displacement field in the bar under uniform tension. Both finite element and peridynamic regions are discretized using cubic subdomains with edge lengths of $\Delta = 0.05$ in; see Figure 11. In order to obtain the discrete form of the peridynamic equation of motion, eight integration points are then placed into subdomains of the peridynamic region. The parameter defining the internal length, l, and the cutoff radius, r_c, are chosen to be 0.05 in and 0.125 in, respectively.

In order to validate the present results, the bar is also modeled using only the peridynamic theory and the finite element method. In the case of the finite element model, the SOLID45 brick element of ANSYS is utilized, and the uniaxial tension is applied as surface tractions at the end surfaces of the bar. The comparison of the displacements among the present coupled analysis, the peridynamic theory, and the finite element method is shown in Figure 12. There is approximately a 5% difference between the models using only the peridynamic theory and finite element method. Furthermore, the peridynamic theory cannot capture Poisson's ratio exactly as explained in [Kilic 2008]. Hence, a small jump is observed at the intersection of the peridynamic and finite element regions.

4.2. *Plate with a circular cutout.* Figure 13 describes the geometry of the plate with a circular cutout. The length and width of the plate are specified as $a = 9$ in and $b = 3$ in respectively. The thickness of the plate has a value of $t = 0.2$ in and the circular cutout has a radius of $r = 0.4$ in. The plate is isotropic
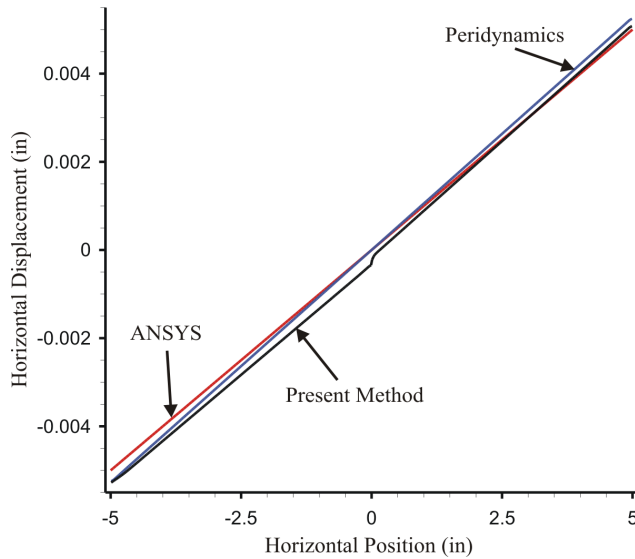
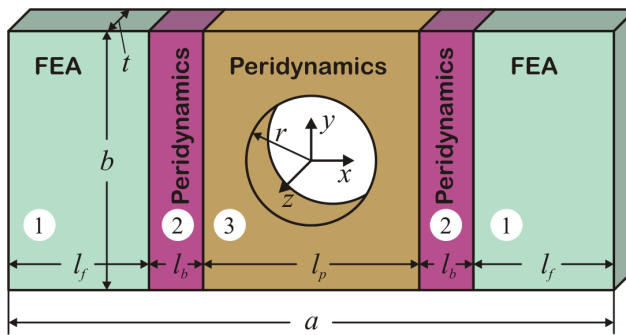**Figure 12.** Comparison of horizontal displacements of the bar.

Figure 13. Dimensions of the plate with a circular cutout.

with Young's modulus and Poisson's ratio of $E = 10^7$ psi and $\mu = 0.25$, respectively. Furthermore, the critical stretch, s_0, is assumed to be 0.0025. The plate is partitioned into five regions, as shown in the figure. The finite element method is employed to model the regions, which are labeled 1; the length, l_f, of these regions is specified to be 2.5 in. The regions labeled as 2 and 3 in Figure 10 are modeled by employing the peridynamic theory; the lengths of these regions are chosen to be $l_b = 0.5$ in and $l_p = 3$ in, respectively. Because of the expected errors near the peridynamic and finite element boundaries, damage is not allowed in region 2 in order to avoid premature failures near these boundaries.

The three-dimensional model is constructed by discretizing the domain into subdomains, as shown in Figure 14. Subdomains are hexahedron shaped with edge lengths of approximately 0.05 in. Hence, the internal length, l, and the cutoff radius, r_c, are chosen to be 0.05 in and 0.125 in, respectively. An integration scheme using eight collocation (integration) points is employed for the peridynamic regions.
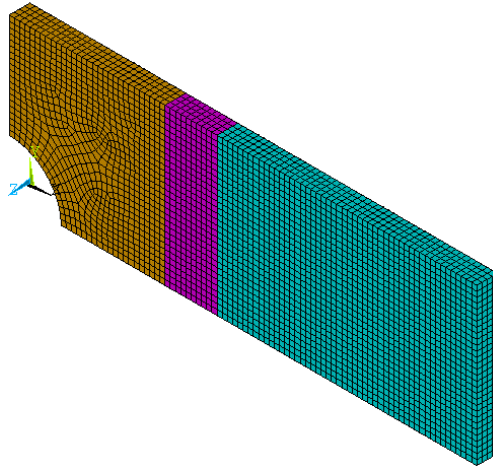
Figure 14. Discretization of the plate with a circular cutout.

The validity of the peridynamic predictions is first established in the absence of failure by comparing the steady-state displacements against the peridynamic theory and the finite element method using AN-SYS, a commercially available program. In the case of no failure, the plate is subjected to a uniaxial tension of 6000 lb. Also, the plate is free of any displacement constraints. Both the peridynamic and finite element models are constructed by utilizing the same discretization as that of the peridynamic model shown in Figure 14. In the case of the peridynamic model, the tensile load is applied through a uniform body force over the volumes having the length 0.05 in. Hence, the value of the body force corresponds to 2.0×10^5 lb/in^3. In the case of the finite element model, the SOLID45 brick elements of ANSYS are utilized to approximate the displacements. The uniaxial tension is applied through surface tractions of 1.0×10^4 lb/in^2. In the case of coupled analysis, the tensile load is applied by using uniform point forces at the nodes located at $x = \pm a/2$ and their values are determined by dividing applied tension by the number of nodes located at $x = \pm a/2$.

Figure 15 shows the horizontal and vertical displacements along the bottom line of the plate. The comparison of horizontal displacements indicates a close agreement (Figure 15, left). Although there is also good correlation of the vertical displacements obtained from the coupled analysis, the peridynamic theory, and the finite element method (Figure 15, right), the deviation is more significant for vertical displacements than for horizontal displacements. The vertical displacements from the coupled analysis and peridynamic methods are in agreement near the cutout since both methods use the peridynamic theory in this region. However, the finite element results display a larger deviation because the Poisson's ratio of 0.25 is not exactly satisfied for thin plates, as explained in [Kilic 2008]. For the same reason, a small jump is observed near the boundary between regions 1 and 2.

The plate with a circular cutout is further investigated for failure simulation. Most experiments involving failure are performed under quasistatic conditions. Therefore, it may not be practical to solve quasistatic problems using standard explicit time integrators because explicit time integrations often require very small time steps, limiting the total time of the simulation. Therefore, the adaptive dynamic relaxation is used to simulate failure.
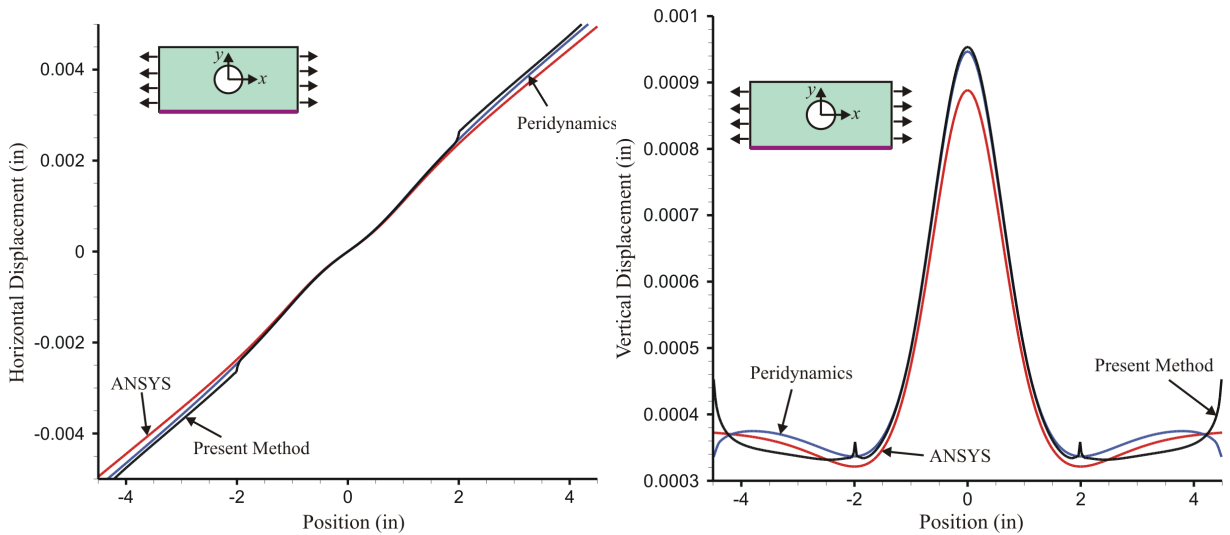
Figure 15. Horizontal (left) and vertical (right) displacements along the bottom line.

As explained in [Kilic 2008], the loading rate might significantly affect the failure patterns since the dynamic problems locally reach higher displacement gradients than under quasistatic conditions because of the traveling elastic waves.

In order to circumvent premature failure due to high local displacement gradients, the tensile load is gradually applied by incrementing the displacement at each iteration of the adaptive dynamic relaxation with a constant value of 3.125×10^{-8} in. This is a small enough value that does not create high local displacement gradients. As evidenced with this type of loading, the plate is subjected to constant displacement, and that they are applied on nodes located at $x = \pm a/2$. Furthermore, the resulting damage pattern in the peridynamic region is illustrated in Figure 16 as a contour plot of local damage given by (5). As expected, the crack initiates at the cutout, near which high displacement gradients exist (Figure 16, top left), and then propagates toward the edges of the plate (top right), until ultimate failure of the plate (bottom). The local damage index in Figure 14 is computed by (5). The local damage being 0.5 is fairly good indicator of material separation. In Figure 16, the local damage value of 0.38 indicates extensive damage not necessarily material separation.

5. Conclusions

Coupling between the peridynamic theory and finite element method was presented in order to take advantage of both methods. Since the finite element is numerically more efficient than the peridynamic theory, the regions without failure were simulated using the finite element method. Furthermore, the peridynamic theory was utilized for the regions where material failure was expected. The coupling was introduced by defining an overlap region. Both the peridynamic and finite element equations were used within this region. Furthermore, the displacement and velocity fields were determined using finite element equations in the overlap region. These fields were then utilized to compute the body force densities using the peridynamic theory. Finally, these body force densities served as external forces for finite elements in the overlap region.
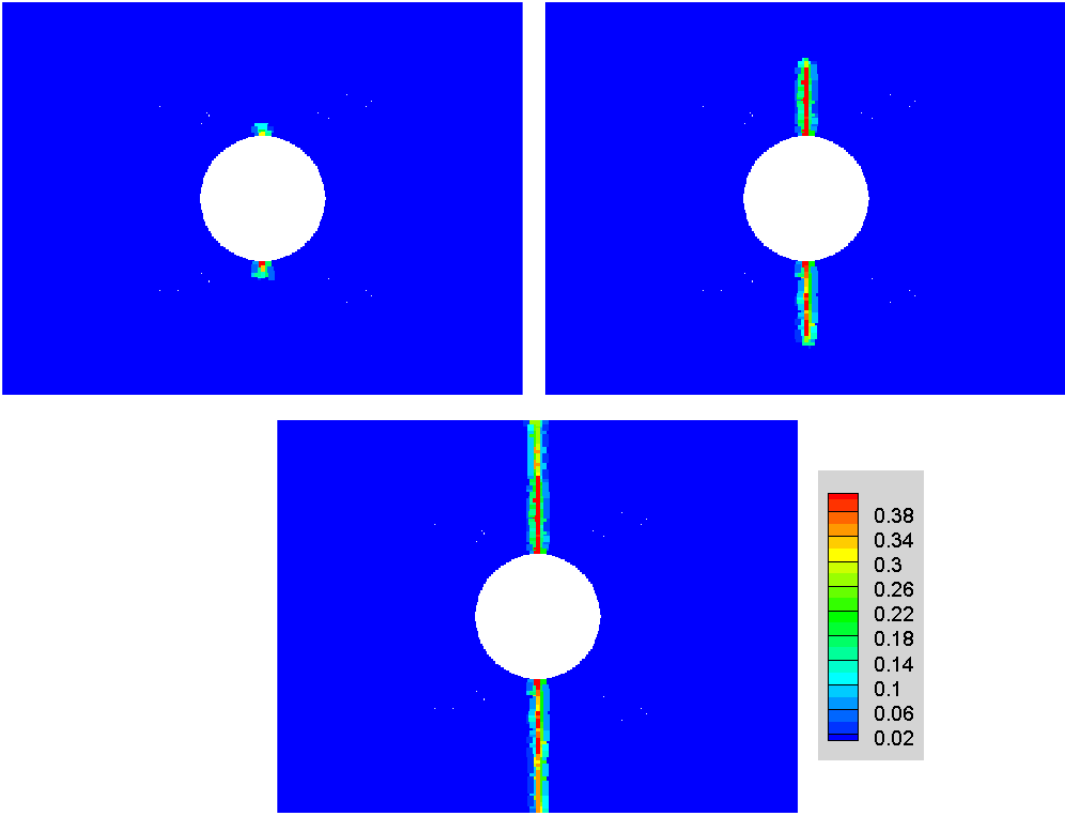
Figure 16. Contour plot of local damage. Clockwise from top left: crack initiation, crack propagation, and ultimate failure. The color scale is the same for each plot.

Material points near free surfaces and interfaces experience increases or decreases in material stiffness since the response function is obtained with the assumption that a point and its surrounding points have the same material properties. Thus, surface corrections are introduced through application of uniform extensions. It is also showed that the Poisson's ratio is not $\frac{1}{4}$ for problems having a thickness less than the cutoff radius. The results showed that the Poisson's ratio is close to $\frac{1}{3}$ for very thin plates and it approaches $\frac{1}{4}$ with increasing plate thickness. However, the surface correction method uses a Poisson's ratio of $\frac{1}{4}$ regardless of the plate thickness, which resulted in a numerical error for thin plates. The effects of internal length and cutoff radius were also investigated. It was found that internal length has a lower bound due to the discretization. Results indicate that the smallest internal length should be in the range of the edge length of the subdomains for integration schemes using eight integration points. The cutoff radius needs to be larger than 2.5 times the internal length for accurate volume integration.

The present approach has been validated by considering a bar with a square cross section and a rectangular plate with a circular cutout, both under tension. In the case of the bar, steady-state displacements were determined for the coupled problem and compared against predictions of the peridynamic theory and finite element method. Comparisons indicate very good agreement but a small displacement jump was observed at the intersection of the peridynamic and finite element regions because the peridynamic

theory does not exactly satisfy its theoretical Poisson's ratio of 0.25. In the case of the plate with the cutout, the steady-state results show trends similar to the bar problem when compared against predictions of the peridynamics and finite element methods. The failure simulation was also performed for a plate with a cutout. As expected, two cracks initiated at the cutout and they propagated with increasing tensile load until ultimate failure of the plate.

Appendix A

The correction factor is determined based on the application of uniaxial tensile loadings to the actual finite domain of interest and the infinite domain. As illustrated in Figure A1, the correction procedure first involves the application of uniaxial tension in the x-direction, and the resulting displacement field can be expressed at the point x as

$$\boldsymbol{u}^T(\boldsymbol{x}) = \left\{ \frac{\partial u^*}{\partial x} x \quad -\nu \frac{\partial u^*}{\partial x} y \quad -\nu \frac{\partial u^*}{\partial x} z \right\}^T, \tag{A1}$$

in which $\partial u^*/\partial x$ is the applied constant displacement gradient. The Poisson's ratio $\nu = 0.25$ because the response function given in (2) is restricted to a pairwise interaction.

Based on numerical experimentation with varying values of displacement gradients, there exists no significant effect on the surface corrections. Thus, the displacement gradient, $\partial u^*/\partial x$ is assigned a value of 0.001. The contractions in the y- and z-directions are ν times the applied displacement gradient, $\partial u^*/\partial x$.

The force density in the x-direction, $g_x(\boldsymbol{x})$, due to the applied displacement gradient given in (A1) is expressed as

$$g_x(\boldsymbol{x}) = \left(\int_{\Omega^+} dV' \boldsymbol{f}(\boldsymbol{u}', \boldsymbol{u}, \boldsymbol{x}', \boldsymbol{x}) - \int_{\Omega^-} dV' \boldsymbol{f}(\boldsymbol{u}', \boldsymbol{u}, \boldsymbol{x}', \boldsymbol{x}) \right)_x, \tag{A2}$$
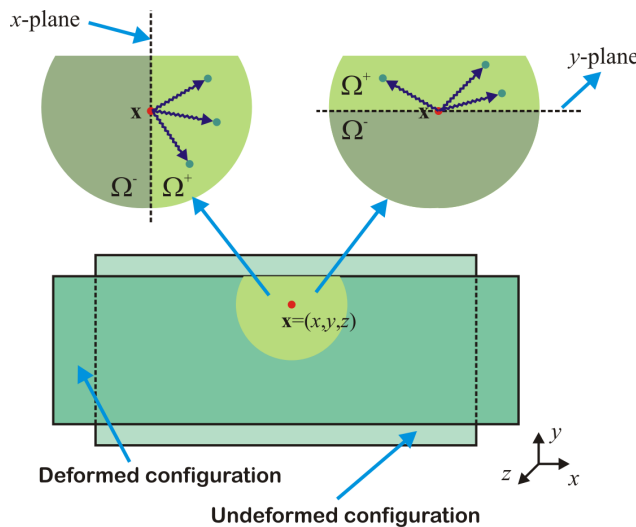
Figure A1. Schematic showing the application of uniaxial tension in the x-direction.

where Ω^+ and Ω^- are the volumes in which integration is performed and are defined to be the right and left sides of the x-plane (Figure A1). The subscript x indicates the x- component of the resulting volume integration. For a point, $\boldsymbol{x}$ embedded in a single material, the value of $g_x(\boldsymbol{x})$ will become 2.

Moreover, by applying the displacement gradient in the y-direction, the force density, $g_y(\boldsymbol{x})$, can written as

$$g_y(\boldsymbol{x}) = \left(\int_{\Omega^+} dV' \boldsymbol{f}(\boldsymbol{u}', \boldsymbol{u}, \boldsymbol{x}', \boldsymbol{x}) - \int_{\Omega^-} dV' \boldsymbol{f}(\boldsymbol{u}', \boldsymbol{u}, \boldsymbol{x}', \boldsymbol{x}) \right)_y, \tag{A3}$$

where Ω^+ and Ω^- are the volumes in which integration is performed; they are defined to be the upper and lower sides of the y-plane (Figure A1). The force densities, $g_x(\boldsymbol{x})$ and $g_y(\boldsymbol{x})$, are clearly different due to dissimilar volumes of integrations. Hence, the domain under uniaxial tension exhibits directional dependence. In other words, depending on the direction of uniaxial tension, the points closer to the free surfaces or interfaces experience different force densities, which is not physically acceptable. Therefore, the uniaxial tension is also applied in the y- and z-directions, which leads to three different responses at each integration point and can be expressed in vector form

$$\boldsymbol{g}^T(\boldsymbol{x}) = \left\{ g_x \quad g_y \quad g_z \right\}, \tag{A4}$$

in which x, y, and z represent the directions of applied uniaxial tension.

It is assumed that there is a fictitious domain composed of a single material (Figure A2). The material in this domain is assumed to have the same properties as those given for point x of the actual domain of interest (Figure A1). As illustrated in Figure A2, the point located at $\boldsymbol{x}^T = \{0, 0, 0\}$ is surrounded by other points so that there is no surface within the cutoff radius, r_c. Hence, this point does not show any directional dependence, and it is sufficient to apply uniaxial tension only in one direction. In order to compute the force density due to uniaxial tension given in (A1), the fictitious domain is discretized using cubic subdomains (Figure A2). The edge length of the cube, Δ_∞, is typically chosen to be one fiftieth of the cutoff radius, r_c. Furthermore, the displacement field is assumed to be constant within each
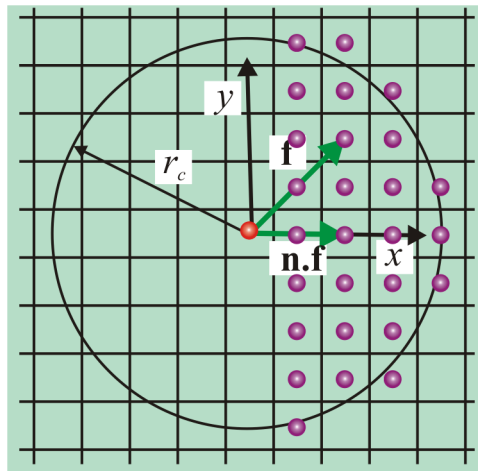
Figure A2. Discretization of infinite domain with cubes.

subdomain. Under these considerations, the force density in this domain can be approximated as,

$$g_\infty = 2 \sum_{i=0}^{\infty} \sum_{j=0}^{\infty} \sum_{k=0}^{\infty} n_x . f(u = 0, u', x', x = 0, t) \Delta_\infty^3, \tag{A5}$$

in which n_x is the unit vector in the x-direction. The position vector x' is defined as

$$x' = \Delta_\infty \{i + \tfrac{1}{2} \quad j + \tfrac{1}{2} \quad k + \tfrac{1}{2}\}^T = \{x' \quad y' \quad z'\}^T. \tag{A6}$$

Finally, the displacement vector u' can be written as

$$u' = \left\{ \frac{\partial u^*}{\partial x} x' \quad -v \frac{\partial u^*}{\partial x} y' \quad -v \frac{\partial u^*}{\partial x} z' \right\}^T. \tag{A7}$$

If the material point is surrounded by material points of the same material and there is no interface or free surfaces within the cutoff radius, which is shown as point 1 in Figure 9, each component of the vector given in (A4) should be equal to the response given in (A5). However, this does not occur due to the approximations in the computation of the integral given in (1). Therefore, the present approach also attempts to correct not only the material stiffness variations due to surface effects but also the approximations in the numerical integration. Therefore, the correction is applied to all collocation points regardless of their position.

As illustrated in Figure A3, the scaling constant g_{ij} between the pair of material points located at x_i and x_j is calculated by assuming an ellipsoidal variation as

$$g_{ij} = \left((n_x/g_{ijcx})^2 + (n_y/g_{ijcy})^2 + (n_z/g_{ijcz})^2 \right)^{-1/2}, \tag{A8}$$

in which n_x, n_y, n_z are the components of the normal vector, n in the undeformed configuration between the pair of material point; it is defined as

$$n = \zeta/|\zeta| = \{n_x, n_y, n_z\}^T. \tag{A9}$$
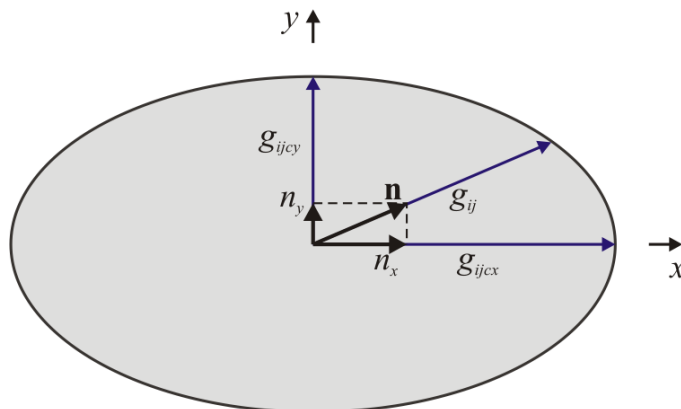
Figure A3. Graphical representation of scaling coefficient.

The average coefficient vector $\boldsymbol{g}_{ijc}$ can be written as

$$\boldsymbol{g}_{ijc} = (\boldsymbol{g}_{ci} + \boldsymbol{g}_{cj})/2, \tag{A10}$$

in which

$$\boldsymbol{g}_c^T(\boldsymbol{x}) = \{g_{xc}, g_{yc}, g_{zc}\} = \{g_\infty/g_{xc}, g_\infty/g_{yc}, g_\infty/g_{zc}\}. \tag{A11}$$

After considering the surface effects, the discrete form of the equations of motion given in (9) is corrected as

$$\rho\ddot{\boldsymbol{u}}(\boldsymbol{x}_i, t) = \boldsymbol{b}(\boldsymbol{x}_i, t) + \sum_{e=1}^{N}\sum_{j=1}^{N_e} g_{ij} w_j \boldsymbol{f}\left(\boldsymbol{u}(\boldsymbol{x}_i, t), \boldsymbol{u}(\boldsymbol{x}_k', t), \boldsymbol{x}_i, \boldsymbol{x}_k', t\right). \tag{A12}$$

According to (A10), the vector $\boldsymbol{g}_{ijc}$ is computed by taking the average of the coefficients given in (A11) for two interacting material points. As a result, the surface correction given in (A8) is underestimated for the material point with the larger scaling coefficient and overestimated for the material point with the smaller scaling coefficient. Hence, a single iteration is generally not sufficient to determine the scaling coefficients. Therefore, the scaling coefficients in (A10) are computed iteratively. Each component given in (A10) is set to unity at the beginning of the first iteration step, and then the method outlined above is utilized to determine the coefficients given in (A10). Then, the present method is repeated n times, during which the results of the previous iteration are used as a scaling coefficient. After numerical investigation, it was found that the change in the coefficients in (A10) is insignificant after approximately twenty iterations. Hence, the number of iterations, n, is taken to be twenty in this study. Although this method enables the correction to material behavior due to the surface effects and approximations during the numerical integration, it is still not exact.

Appendix B

The effects of the peridynamic parameters and discretization are established by considering a rectangular plate (Figure B1). The length and width of the plate are specified as $a = 10$ in and $b = 4$ in, respectively. The plate is free of any displacement constraints and is subjected to uniaxial tension in the x-direction.
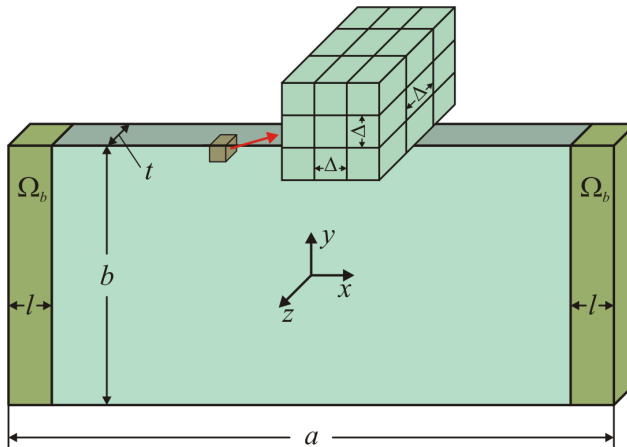
Figure B1. Dimensions and discretization of the plate.

However, point and surface loads cannot be applied directly because the peridynamic equation of motion involves a volume integral that gives rise to zero for point and surface loads. Thus, the uniaxial tension is applied as uniform body forces over the volumes, Ω_b, along the vertical edges having a length, l, of 0.08 in (Figure B1). The longitudinal component of the applied body force is specified as $b_x = 234375.0 \, \text{lb/in}^3$. Hence, the applied tension, F, can be computed in terms of the plate dimensions as $F = lbtb_x$.

The material of the plate is isotropic with Young's modulus and Poisson's ratio of $E = 10^7$ psi and $v = 0.25$, respectively. The three-dimensional peridynamic model is constructed by discretization of the plate using cubic subdomains (Figure B1). In each subdomain, eight integration points are utilized to reduce the peridynamic equation of motion to its discrete form. The steady-state solutions are obtained by using the adaptive dynamic relaxation.

Within the realm of molecular dynamics, it is well known that the Poisson's ratio is restricted to $\frac{1}{4}$ in three dimensions and $\frac{1}{3}$ in two dimensions if atomic interactions are pairwise and do not exhibit any directional dependence. Gerstle et al. [2005] showed that the same restrictions apply to peridynamics equations under the same conditions. Hence, the thickness of the plate affects the observed Poisson's ratio. Figure B2 shows the variation of the Poisson's ratio with increasing plate thickness. The Poisson's ratio is calculated using steady-state displacements at the point located at x_0, which can be expressed as

$$x_0^T = \{x_0 = 2.5, \, y_0 = 1.0, \, z_0 = 0.0\} \tag{B1}$$

and the displacement field at x_0 can be written as

$$u_0^T = \{u_{x0}, u_{y0}, u_{z0}\}. \tag{B2}$$

Hence, the Poisson's ratio is approximated by using initial positions and displacements as

$$v = -\frac{u_{y0}/y_0}{u_{x0}/x_0}. \tag{B3}$$
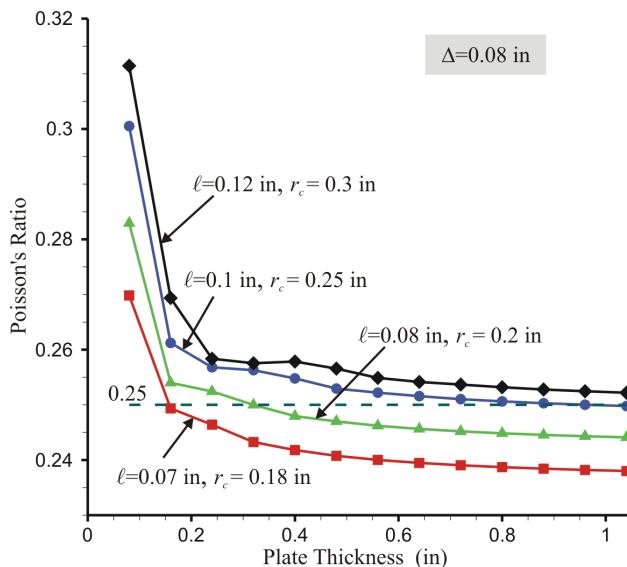
Figure B2. Effect of internal length on Poisson's ratio with increasing plate thickness.

It is apparent in Figure B2 that the Poisson's ratio approaches its theoretical value of $\frac{1}{4}$ with increasing plate thickness. Conversely, the Poisson's ratio approaches $\frac{1}{3}$ with decreasing plate thickness. The internal length also affects the Poisson's ratio substantially (Figure B2). The number of interactions for points shown in Figure 9 can be determined by finding the volume of points whose distance to point of interest is less than the cutoff radius. Hence, the number of interactions for a point located at x can be computed as

$$\chi(x) = \int_{|x'-x|<r_c} dV_{x'}. \tag{B4}$$

According to (B4), a point can have the highest number of interactions if it is completely surrounded by other points within the range of the cutoff radius. Hence, the highest number of interactions is the volume of a sphere, which can be expressed as

$$\chi_{\max} = \frac{4}{3}\pi r_c^3. \tag{B5}$$

For thin structures whose thickness is less than the cutoff radius, $\chi_{\max}$ is never reached. Furthermore, the ratio of the number of interactions to $\chi_{\max}$ reduces with increasing internal length due to its proportionality with the cutoff radius. Therefore, the plate behaves more like a two-dimensional medium with increasing internal length since most interactions are in the x-y plane. As a result, the Poisson's ratio increases with increasing internal length, especially for thin plates (Figure B2).

It is also expected that the plate thickness affects the displacement fields because the surface correction is based on the assumption that the Poisson's ratio is $\frac{1}{4}$. However, the Poisson's ratio is not necessarily $\frac{1}{4}$ for thin structures (Figure B2). Thus, longitudinal displacements deviate from the results of the finite element analysis with decreasing plate thickness (Figure B3, left). The finite element results are obtained using SOLID45 brick elements of ANSYS. The three-dimensional finite element mesh is constructed
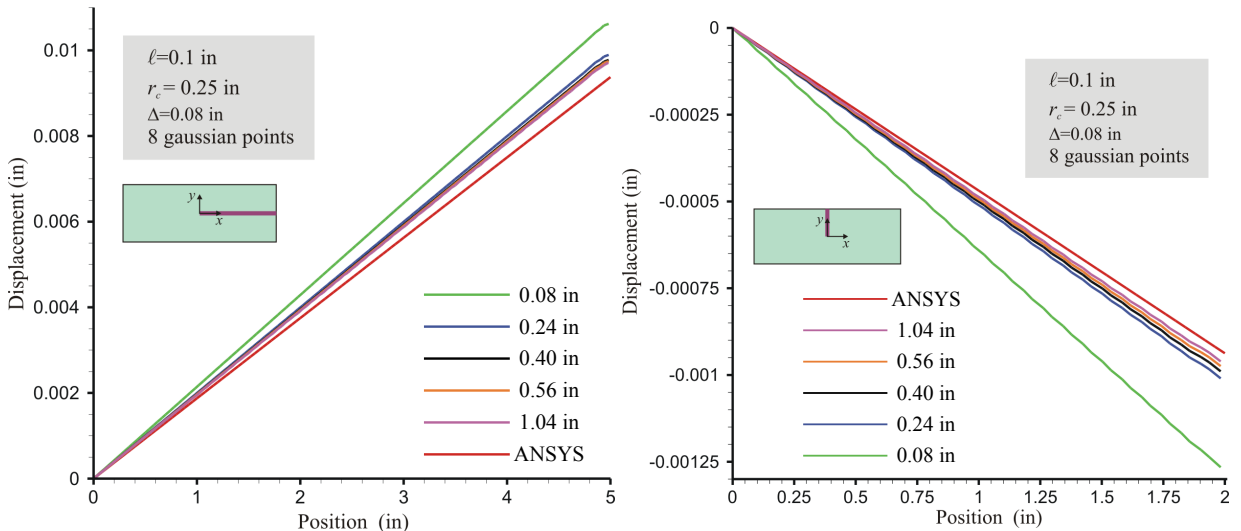
Figure B3. Effect of layer thickness on displacements in the x-direction (left) and the y-direction (right). In each graph, the curves are stacked in the same order as in the legend.
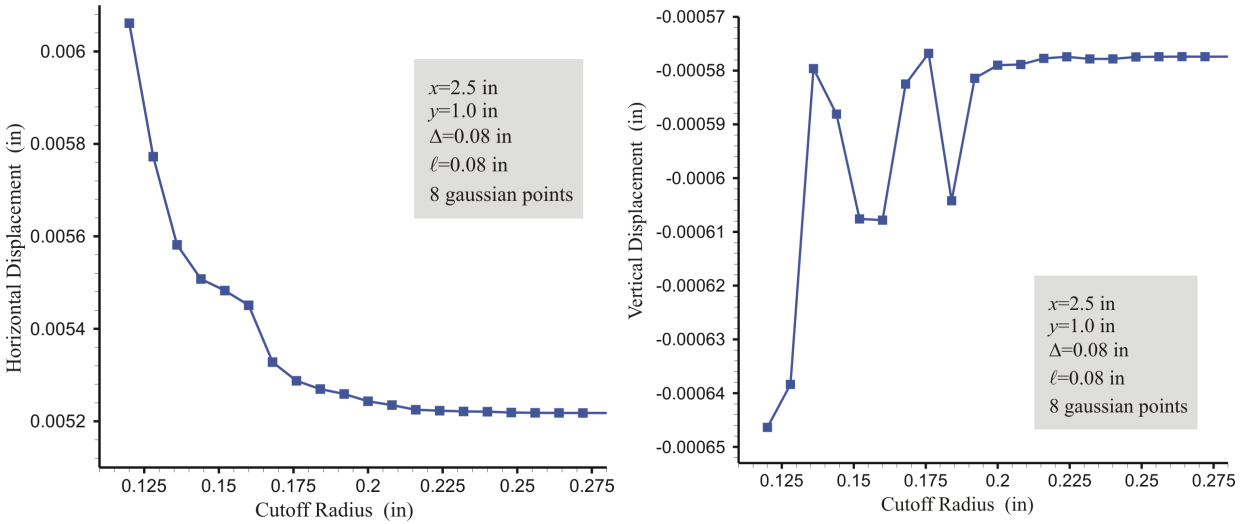
Figure B4. Effect of cutoff radius on displacements in the x-direction (left) and the y-direction (right).
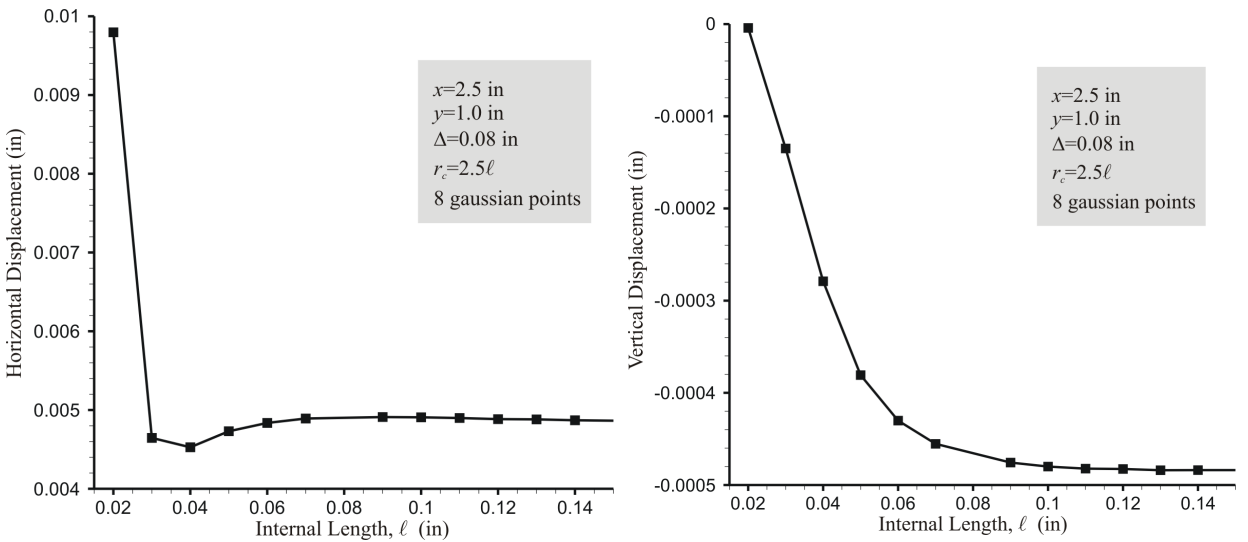
Figure B5. Effect of internal length on displacements in the x-direction (left) and the y-direction (right).

using the discretization shown in Figure B1, and the Poisson's ratio is specified as $\frac{1}{4}$. The differences in results are more pronounced for displacements in the transverse direction (Figure B3, right) because they are influenced by both the surface correction and the Poisson's ratio. However, the results converge to that of the finite element method with increasing plate thickness (Figure B3).

Determination of the internal length and cutoff radius for a specific problem is another source of uncertainty or approximation. The computational resources typically limit the number of subdomains.

This limitation might be due to the available computational space and/or memory. However, the primary limitation on the number of subdomains is the total computational time, which depends on the number of time steps. The computational time can be minimized by using the smallest possible cutoff radius for a given discretization. On the contrary, the accuracy of numerical integration provides a lower bound for the cutoff radius. Here, in order to quantify the effect of the cutoff radius on the numerical predictions, the internal length is specified as 0.08 in and the cutoff radius is varied. Figure B4 shows the change in displacements at the point located at $\{2.5 \quad 1.0 \quad 0.0\}^T$ with an increasing cutoff radius. In this case, the plate thickness is defined as 0.08 in. The volume integral given in (1) is performed over the domain (Figure B1). However, the cutoff radius is introduced to reduce the computational time by taking advantage of the rapidly decaying exponential term in the response function. For a small cutoff radius, the volume integration is not performed accurately because the exponential term is still significant beyond the cutoff radius. Therefore, some of the stiffness of the material is lost, resulting in high longitudinal displacements (Figure B4, left). However, the longitudinal displacement converges with increasing cutoff radius (Figure B4). When the cutoff radius is larger than 0.2 in, no significant difference is observed in the displacement results. The cutoff radius of 0.2 is 2.5 times the internal length. Therefore, the present study utilizes a cutoff radius that is 2.5 times the internal length for the remaining computations.

After determining the cutoff radius in terms of the internal length, the internal length is also varied for a plate with a thickness of 0.8 in. Figure B5 shows the variation of the displacements at the point located at $\{2.5 \quad 1.0 \quad 0.0\}^T$ with an increasing internal length. As expected, the numerical integration is not accurate for a small internal length because the exponential term decays very fast. A material point is mostly influenced by the nearest points, for which the exponential term is very small. For small internal length, there is also a loss in stiffness of the material since most of the stiffness is localized near the material point that is not captured by the numerical integration correctly. However, the displacements converge with increasing internal length. Results do not significantly change for internal lengths larger than 0.08 in. This specific value is the size of the cubic subdomain in the discretization and the present study utilizes the highest edge length of the subdomains as the internal length.

References

[Askari et al. 2006] E. Askari, J. Xu, and S. Silling, "Peridynamic analysis of damage and failure in composites", in *44th AIAA Aerospace Sciences Meeting and Exhibit* (Reno, NV, 2006), AIAA, Reston, VA, 2006. Paper #2006-88.

[Bathe 1982] K. J. Bathe, *Finite element procedures in engineering analysis*, Prentice-Hall, Englewood Cliffs, NJ, 1982. Revised in 1996.

[Belytschko 1983] T. Belytschko, "An overview of semidiscretization and time integration procedures", pp. 1–65 in *Computational methods for transient analysis*, edited by T. Belytschko and T. J. R. Hughes, North-Holland, Amsterdam, 1983.

[Belytschko and Black 1999] T. Belytschko and T. Black, "Elastic crack growth in finite elements with minimal remeshing", *Int. J. Numer. Methods Eng.* **45**:5 (1999), 601–620.

[Berger and Bokhari 1987] M. J. Berger and S. H. Bokhari, "A partitioning strategy for nonuniform problems on multiprocessors", *IEEE Trans. Comput.* **C-36**:5 (1987), 570–580.

[Colavito et al. 2007a] K. W. Colavito, B. Kilic, E. Celik, E. Madenci, E. Askari, and S. Silling, "Effect of void content on stiffness and strength of composites by a peridynamic analysis and static indentation test", in *48th AIAA/ASME/ASCE/AHS/ASC Structures, Structural Dynamics, and Materials Conference* (Honolulu, HI, 2007), AIAA, Reston, VA, 2007. Paper #2007-2251.

[Colavito et al. 2007b] K. W. Colavito, B. Kilic, E. Celik, E. Madenci, E. Askari, and S. Silling, "Effects of nanoparticles on stiffness and impact strength of composites", in *48th AIAA/ASME/ASCE/AHS/ASC Structures, Structural Dynamics, and Materials Conference* (Honolulu, HI, 2007), AIAA, Reston, VA, 2007. Paper #2007-2021.

[Gerstle and Sau 2004] W. H. Gerstle and N. Sau, "Peridynamic modeling of concrete structures", pp. 949–956 in *Fracture mechanics of concrete structures: proceedings of the Fifth International Conference on Fracture Mechanics of Concrete and Concrete Structures* (Vail, CO, 2004), vol. 2, edited by V. C. Li et al., Ia-FraMCos, Evanston, IL, 2004.

[Gerstle et al. 2005] W. Gerstle, N. Sau, and S. Silling, "Peridynamic modeling of plain and reinforced concrete structures", pp. 54–68 in *Proceedings of the 18th International Conference on Structural Mechanics in Reactor Technology* (*SMiRT 18*) (Beijing, 2005), edited by Y. Zhou et al., Atomic Energy Press, Beijing, 2005. Paper #SMiRT18-B01-2.

[Jirásek 2000] M. Jirásek, "Comparative study on finite elements with embedded discontinuities", *Comput. Methods Appl. Mech. Eng.* **188**:1–3 (2000), 307–330.

[Kilic 2008] B. Kilic, *Peridynamic theory for progressive failure prediction in composite materials*, Ph.D. thesis, University of Arizona, Tucson, AZ, 2008.

[Macek and Silling 2007] R. W. Macek and S. A. Silling, "Peridynamics via finite element analysis", *Finite Elem. Anal. Des.* **43**:15 (2007), 1169–1178.

[Melenk and Babuška 1996] J. M. Melenk and I. Babuška, "The partition of unity finite element method: basic theory and applications", *Comput. Methods Appl. Mech. Eng.* **139**:1–4 (1996), 289–314.

[Moës and Belytschko 2002] N. Moës and T. Belytschko, "Extended finite element method for cohesive crack growth", *Eng. Fract. Mech.* **69**:7 (2002), 813–833.

[Moës et al. 1999] N. Moës, J. Dolbow, and T. Belytschko, "A finite element method for crack growth without remeshing", *Int. J. Numer. Methods Eng.* **46**:1 (1999), 131–150.

[Silling 2000] S. A. Silling, "Reformulation of elasticity theory for discontinuities and long-range forces", *J. Mech. Phys. Solids* **48**:1 (2000), 175–209.

[Silling 2003] S. A. Silling, "Dynamic fracture modeling with a meshfree peridynamic code", pp. 641–644 in *Second MIT Conference on Computational Fluid and Solid Mechanics* (Cambridge, MA, 2003), edited by K. J. Bathe, Elsevier, Amsterdam, 2003.

[Silling and Askari 2004] S. A. Silling and E. Askari, "Peridynamic modeling of impact damage", *ASME Conf. Proc.* **2004** (2004), 197–205. Paper No. PVP2004-3049.

[Silling and Askari 2005] S. A. Silling and E. Askari, "A meshfree method based on the peridynamic model of solid mechanics", *Comput. Struct.* **83**:17–18 (2005), 1526–1535.

[Silling and Bobaru 2005] S. A. Silling and F. Bobaru, "Peridynamic modeling of membranes and fibers", *Int. J. Non-Linear Mech.* **40**:2–3 (2005), 395–409.

[Underwood 1983] P. Underwood, "Dynamic relaxation", pp. 245–265 in *Computational methods for transient analysis*, edited by T. Belytschko and T. J. R. Hughes, North-Holland, Amsterdam, 1983.

[Xu et al. 2007] J. Xu, A. Askari, O. Weckner, H. Razi, and S. Silling, "Damage and failure analysis of composite laminates under biaxial loads", in *48th AIAA/ASME/ASCE/AHS/ASC Structures, Structural Dynamics, and Materials Conference* (Honolulu, HI, 2007), AIAA, Reston, VA, 2007. Paper #2007-2315.

[Zi et al. 2007] G. Zi, T. Rabczuk, and W. Wall, "Extended meshfree methods without branch enrichment for cohesive cracks", *Comput. Mech.* **40**:2 (2007), 367–382.

[Zienkiewicz 1977] O. C. Zienkiewicz, *The finite element method*, 3rd ed., McGraw-Hill, London, 1977. 6th ed. published in 2005.

BAHATTIN KILIC: bkilic@gmail.com
Department of Aerospace and Mechanical Engineering, The University of Arizona, Tucson, AZ 85716, United States

ERDOGAN MADENCI: madenci@email.arizona.edu
Department of Aerospace and Mechanical Engineering, The University of Arizona, Tucson, AZ 85716, United States
http://www.ame.arizona.edu/faculty/madenci/madenci.php

JOURNAL OF MECHANICS OF MATERIALS AND STRUCTURES

Journal of Mechanics of Materials and Structures